Received June 14, 2020, accepted July 6, 2020, date of publication July 9, 2020, date of current version July 21, 2020.

Digital Object Identifier 10.1109/ACCESS.2020.3008176

A Comparative Study of Inversion Optimization Algorithms for Underground Metal Target Detection

YADONG WAN[1], ZHEN WANG[1], PENG WANG[1,2], CHAO ZHANG[3], SHIHONG DUAN[1], AND NA LI[4]

[1]School of Computer and Communication Engineering, University of Science and Technology Beijing, Beijing 100083, China
[2]Datang Gohigh Data Networks Technology Company Ltd., Beijing 100191, China
[3]School of Materials Science and Engineering, University of Science and Technology Beijing, Beijing 100083, China
[4]School of Mathematics and Physics, University of Science and Technology Beijing, Beijing 100083, China

Corresponding author: Peng Wang (wangpeng.micl@gmail.com)

This work was supported in part by the China Postdoctoral Science Foundation under Grant 2019M650778, in part by the Fundamental Research Funds for the Central Universities under Grant 2302018FRF-GF-18-016B, in part by the National Natural Science Foundation of China (NSFC) Project under Grant 61671056, and in part by the China Education and Research Network (CERNET) of China through CERNET Innovation Project under Grant NGII20160304.

ABSTRACT Underground metal target detection refers to estimating the properties of underground metal targets based on a set of observed data. Electromagnetic induction (EMI) method and the least-squares inversion provide the data acquisition method and the parameter estimation method for the detection, respectively. As an important part of least-squares inversion, optimization algorithms directly affect the efficiency of the least-squares inversion. To improve the efficiency of underground metal target detection, it is necessary to compare the performance of different optimization algorithms. In this paper, we analyzed the characteristic of the complex EMI forward model using sensitivity analysis and inverse sensitivity analysis at first. Then, the EMI forward model and least squares were used to build the objective function. The estimation error, run time and number of iterations of six numerical optimization algorithms were compared under different signal-to-noise ratios (SNRs) and under different data acquisition spacing. The algorithms include gradient descent, steepest descent, Newton's method, Broyden-Fletcher-Goldfarb-Shanno (BFGS) algorithm, conjugate gradient method and Levenberg–Marquardt (LM) algorithm. A simulation platform was established to generate observed data and compare the optimization algorithms. The results of algorithm comparison showed that the BFGS, conjugate gradient and LM algorithm can efficiently and accurately estimate the properties of underground metal targets and the LM algorithm has the shortest run time and the least number of iterations. Finally, we carefully analyzed the time consumption of each optimization algorithm. The results show that the calculation of the gradient and step length selection greatly affect the efficiency of the optimization algorithms.

INDEX TERMS Electromagnetic induction (EMI), least-squares inversion, optimization algorithm, sensitivity analysis, underground metal target detection.

I. INTRODUCTION

As one of the geophysical inversion problems, underground metal target detection aims to estimate the properties of underground metal targets based on a set of observed data and it has been widely implemented in military, archeology, prospecting, and many other fields [1]–[4]. In underground metal target detection, the observed data are usually collected by the electromagnetic induction (EMI) method [5]–[7]. The EMI method uses the induced magnetic fields generated by underground metal targets as observed data. Based on the observed data, the properties of underground metal targets can be estimated by inversion algorithms [8]–[10]. With the wide application of underground metal target detection, the demand for efficient inversion algorithms is also increasing.

The associate editor coordinating the review of this manuscript and approving it for publication was Larbi Boubchir.

The least-squares inversion is a commonly used inversion algorithm [10], [11]. The least-squares inversion estimates the properties of underground metal targets by minimizing the objective function which measures the misfit between observed values and the fitted values provided by a forward model [12], [13]. The forward model in the EMI method takes the metal target's parameters as input and produces predicted induced magnetic field data [14], [15]. The objective function can be minimized by the numerical optimization algorithms [16]–[19]. The numerical optimization algorithms are iterative and they begin with an initial guess of the optimal values of the parameters and generate a sequence of improved estimates until they reach a solution. Over the last few years, numerical optimization algorithms have been widely used in underground metal target detection. Fernandez *et al.* used the Broyden-Fletcher-Goldfarb-Shanno (BFGS) algorithm for inversion to identify unexploded ordnance based on the man-portable vector sensor data [16]. Grzegorczyk *et al.* used the Gauss–Newton algorithm for underground metal target detection [17]. In the study of Rodi *et al.*, the conjugate gradient method was used to solve the magnetotelluric inverse problem [18]. Marsh *et al.* used the Levenberg–Marquardt (LM) algorithm to find the least-squares solution for the metal target detection [19]. As an important part of the least-squares inversion, numerical optimization algorithms directly affect the efficiency of the inversion process. In order to improve the efficiency of least-squares inversion, it is necessary to compare the performance of common numerical optimization algorithms and analyze the time-consuming calculations during the procedure of these algorithms.

In this paper, we use cylindrical metal targets as the targets to be detected and use the EMI method as the data acquisition method. The purpose of the detection is to estimate the position, principal axes polarizability and orientation of underground cylindrical metal targets. The ordinary forward model and cylinder forward model in the EMI method are introduced at first. Then the sensitivity analysis and the inverse sensitivity analysis of the cylinder forward model are carried out. The sensitivity analysis results show that the distance between the metal target and the detector mostly affects the metal target's EMI response. The inverse sensitivity analysis results indicate that the position of the target estimated by the optimization algorithms is more accurate than that of the principal axes polarizability and orientation. Next, the estimation error, run time and number of iterations of six numerical optimization algorithms are compared under different signal-to-noise ratios (SNRs) and different amounts of observed data. The algorithms include gradient descent, steepest descent, Newton's method, BFGS algorithm, conjugate gradient method and LM algorithm. The comparison results show that the gradient descent and steepest descent take a large amount of time to converge. In the Newton method, the Hessian matrix will be singular in the iterative process, which causes the Newton's method to fail to converge. The BFGS algorithm, conjugate gradient method and LM algorithm can efficiently and accurately estimate the properties of underground metal targets, and the LM algorithm has the shortest run time and the least number of iterations. The simulation results also indicated that the accuracy of the underground metal target detection is greatly affected by noise and the efficiency of the underground metal target detection is greatly affected by the data acquisition spacing. Finally, we carefully analyzed the time consumption of each optimization algorithm. The results show that the gradient calculation and step length selection greatly affect the efficiency of the optimization algorithms. The main contributions of this paper can be summarized as follows:

- The sensitivity analysis and inverse sensitivity are performed to analyze cylinder forward model in underground metal target detection.
- The performances of six numerical optimization algorithms, which include gradient descent, steepest descent, Newton's method, BFGS algorithm, conjugate gradient method and LM algorithm, are compared and the time-consuming calculations in these algorithms are analyzed.

The detailed content of this paper is arranged as follows: we begin in Section 2 by outlining the process of underground metal target detection. Then we introduce the ordinary forward model, cylinder forward model and the objective function. In Section 3, the theoretical description of variance-based sensitivity analysis, inverse sensitivity analysis and numerical optimization algorithms are addressed. The simulation design and the results are given in Section 4. Finally, conclusion comes in Section 5.

II. SYSTEM MODEL

The process of underground metal target detection is shown in Fig. 1. The metal target is located at a specific position in the underground space. Researchers collect the observed data by sequentially placing the EMI detector at different data acquisition positions. The response of a metal target correlates with metal's position, size, shape, orientation and material properties. Based on these observed data and the forward model, the objective function could be constructed.

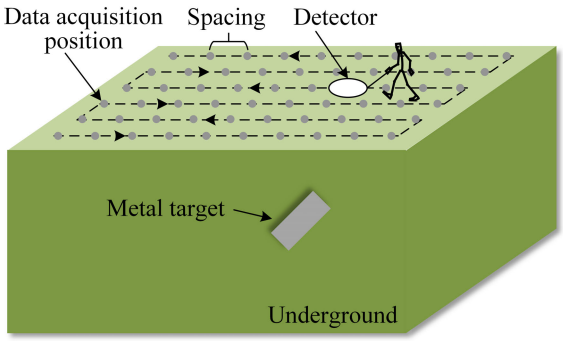

FIGURE 1. Process of underground metal target detection.

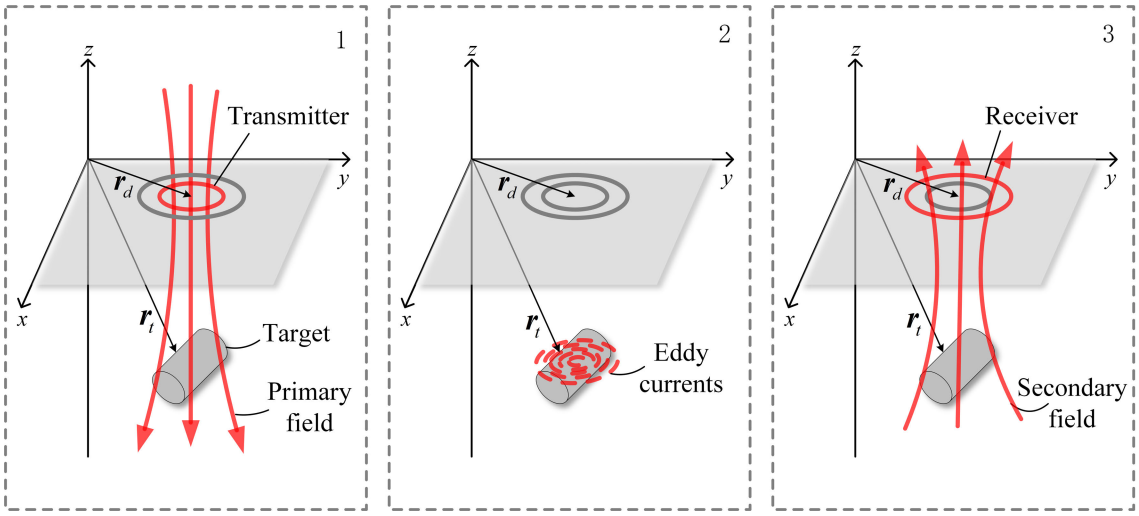

FIGURE 2. EMI response process of the metal target.

A. FORWARD MODEL

The forward model is used to simulate the actual EMI response of metal targets. The process that an underground metal target responds to the electromagnetic field is illustrated in Fig. 2. A typical EMI detector has a transmitter coil and a receiver coil. When the primary field generated by transmitter coil acts on the metal target, the eddy currents will be induced in the metal target. Then the receiver coil could detect the secondary field generated by the eddy currents. An object that could produce a magnetic field is often approximated by a magnetic moment in underground metal detection, and this approximation is valid if the distance from the detector to the metal target is larger than the size of the metal target [20]. The magnetic moment generated by the transmitter coil is [21]:

$$\boldsymbol{m}_p = I_0 \cdot S \cdot \boldsymbol{n} \tag{1}$$

where I_0 is the current amplitude input into the transmitter coil, S is the area of the transmitter coil, $\boldsymbol{n}$ is the direction of the magnetic moment. Suppose that the position vector of the metal target is $\boldsymbol{r}_t$ and the position vector of the detector is $\boldsymbol{r}_d$. The primary field at the metal target position is [1]:

$$\boldsymbol{B}_p = \frac{1}{4\pi}\left[\frac{3\left(\boldsymbol{m}_p^T \boldsymbol{r}_{dt}\right)\boldsymbol{r}_{dt}}{r^5} - \frac{\boldsymbol{m}_p}{r^3}\right] \tag{2}$$

where $\boldsymbol{r}_{dt}$ is the vector from the center of the detector to the center of the object and equals to $\boldsymbol{r}_t - \boldsymbol{r}_d$, r is the norm of $\boldsymbol{r}_{dt}$. The induced magnetic moment generated by the eddy currents is [22]:

$$\boldsymbol{m}_s = \boldsymbol{M}\boldsymbol{B}_p \tag{3}$$

where $\boldsymbol{M}$ is the magnetic polarizability tensor. $\boldsymbol{M}$ is symmetric and can be represented as:

$$\boldsymbol{M} = \begin{bmatrix} M_{11} & M_{12} & M_{13} \\ M_{12} & M_{22} & M_{23} \\ M_{13} & M_{23} & M_{33} \end{bmatrix} \tag{4}$$

In the ordinary forward model, $\boldsymbol{M}$ fully reflects the dipole response of the metal target and its value depends on the size, shape, orientation and material of the metal target. Based on the induced magnetic moment, the secondary field is calculated as [1]:

$$\boldsymbol{B}_s = \frac{\mu_0}{4\pi}\left[\frac{3\left(\boldsymbol{m}_s^T \boldsymbol{r}_{td}\right)\boldsymbol{r}_{td}}{r^5} - \frac{\boldsymbol{m}_s}{r^3}\right] \tag{5}$$

where μ_0 is the vacuum permeability, $\boldsymbol{r}_{td}$ is the vector from the center of the object to the center of the detector and equals to $\boldsymbol{r}_d - \boldsymbol{r}_t$. The ordinary forward model can be expressed as the following function:

$$\boldsymbol{B}_s = g\left(r_{dx}, r_{dy}, r_{dz}, r_{tx}, r_{ty}, r_{tz}, M_{11}, M_{12}, M_{13}, M_{22}, M_{23}, M_{33}\right) \tag{6}$$

where r_{dx}, r_{dy}, r_{dz} are the x, y, z axis coordinates of the detector, and r_{tx}, r_{ty}, r_{tz} are the x, y, z axis coordinates of the metal target.

For axisymmetric cylindrical metal targets, researchers derived a more detailed forward model. Assume that the three principal axes of a cylindrical metal target are shown in Fig. 3. Since $\boldsymbol{M}$ is symmetric, $\boldsymbol{M}$ can be diagonalized by an appropriate rotation of the coordinate [23]:

$$\boldsymbol{M} = \boldsymbol{R}\boldsymbol{\beta}\boldsymbol{R}^T \tag{7}$$

where $\boldsymbol{\beta}$ is the diagonal matrix composed of the eigenvalues of $\boldsymbol{M}$. $\boldsymbol{\beta}$ can be expressed as:

$$\boldsymbol{\beta} = \begin{bmatrix} \beta_x & 0 & 0 \\ 0 & \beta_y & 0 \\ 0 & 0 & \beta_z \end{bmatrix} \tag{8}$$

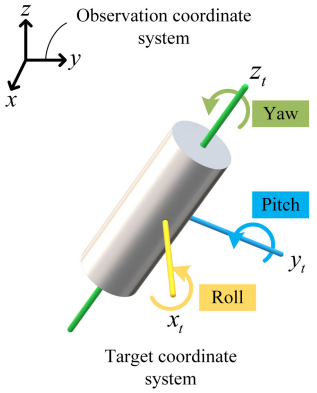

FIGURE 3. Orientation of the cylindrical metal target.

where β_x, β_y, β_z are the three principal axes polarizabilities of the metal target. For a cylindrical metal target with radius a and length L, three principal axes polarizabilities can be calculated empirically as [24]:

$$\beta_x = \beta_y = \frac{1}{2}v\left(0.35 + \frac{\sqrt{j\omega\tau} - 2}{\sqrt{j\omega\tau} + 1}\right) \tag{9}$$

$$\beta_z = \frac{Lv}{4a}\left(\frac{\sqrt{31j\omega\tau} - 2}{\sqrt{31j\omega\tau} + 1} - 0.7\right) \tag{10}$$

where v is the volume of the cylinder and equals to pia^2L, j is the imaginary unit, ω is the angular frequency of the current input in the transmitter coil, τ is the time constant and could be calculated as:

$$\tau = \frac{a^2\sigma\mu}{\mu_r^2} \tag{11}$$

where σ is the conductivity of the metal target, μ and μ_r are the permeability and relative permeability of the metal target, respectively. The $\boldsymbol{R}$ in Formula (7) is the Euler rotation matrix that convert the vector in the object coordinate system to the vector in the observation coordinate system [25]:

$$\boldsymbol{R} = \begin{bmatrix} \sin\theta & 0 & -\sin\theta \\ \sin\theta\sin\varphi & \cos\varphi & \cos\theta\sin\varphi \\ \sin\theta\cos\varphi & -\sin\varphi & \cos\theta\cos\varphi \end{bmatrix} \tag{12}$$

where θ is the pitch angle of the metal target and φ is the roll angle of the metal target. The induced magnetic moment of a cylindrical metal target is expressed as:

$$\boldsymbol{m}_s = \boldsymbol{R}\boldsymbol{\beta}\boldsymbol{R}^T\boldsymbol{B}_p \tag{13}$$

The cylinder forward model can be expressed as the following function:

$$\boldsymbol{B}_s = g\left(r_{dx}, r_{dy}, r_{dz}, r_{tx}, r_{ty}, r_{tz}, \beta_x, \beta_y, \beta_z, \theta, \varphi\right) \tag{14}$$

B. OBJECTIVE FUNCTION

The objective function measures the misfit between observed values and the fitted values provided by the forward model. Suppose that w sets of observed data are collected in an area. These observed data include data acquisition positions $(\boldsymbol{r}_{d1}, \boldsymbol{r}_{d1}, \ldots, \boldsymbol{r}_{dw})$ and corresponding secondary field $(\boldsymbol{B}_{s1}, \boldsymbol{B}_{s2}, \ldots, \boldsymbol{B}_{sw})$. The residuals are the differences between each observed value and the model's predicted value:

$$r_j(\boldsymbol{x}) = \boldsymbol{B}_{sj} - g\left(\boldsymbol{r}_{dj}, \boldsymbol{x}\right), \quad j = 1, 2, \ldots, w \tag{15}$$

where $\boldsymbol{x}$ is the metal target's parameters to be estimated. The objective function is the sum of squares of all residuals:

$$f(\boldsymbol{x}) = \frac{1}{2}\sum_{j=1}^{w} r_j^2(\boldsymbol{x}) \tag{16}$$

The parameters that minimize the value of the objective function are the optimal estimations of the metal target's properties:

$$\boldsymbol{x}^* = \arg\min_{\boldsymbol{x}} f(\boldsymbol{x}) \tag{17}$$

where $\boldsymbol{x}^*$ denotes the optimal estimation of the metal target's parameters.

III. SENSITIVITY ANALYSIS AND NUMERICAL OPTIMIZATION ALGORITHMS

A. SENSITIVITY ANALYSIS

Before optimizing the objective function, we conduct a sensitivity analysis on the cylinder forward model. Because of the complexity of the forward model, the impact of input parameters on output is difficult to understand intuitively. Global sensitivity analysis quantifies the importance of model inputs and their interactions with respect to model output and it is widely used in recent years [26]. For the cylinder forward model, the sensitivity analysis can quantify the importance of the cylindrical metal's parameters to the secondary field.

Variance-based method, as one of global sensitivity analysis, aims at decomposing the variance of the output as a sum of contributions of input parameters [27]–[31]. In variance-based method, total sensitivity indices are usually calculated to quantify the contributions of each input parameter. Consider a model that output is a scalar $Y = g(X_1, X_2, \ldots, X_n)$. The model's input parameter X_i has a uniform distribution over [0, 1]. The variance of the output can be decomposed in the following way using law of total variance [28], [32], [33]:

$$V(Y) = V_{X_{\sim i}}\left(E_{X_i}\left(Y|X_{\sim i}\right)\right) + E_{X_{\sim i}}\left(V_{X_i}\left(Y|X_{\sim i}\right)\right) \tag{18}$$

where X_i denotes the ith input parameter, $X_{\sim i}$ denotes all input parameters but X_i, $E(\cdot)$ and $V(\cdot)$ denote the expectation and variance, $V_{X_{\sim i}}\left(E_{X_i}\left(Y|X_{\sim i}\right)\right)$ represents the contribution of $X_{\sim i}$ and interactions between them to the output variance. The total sensitivity indices are calculated as follows:

$$S_{Ti} = 1 - \frac{V_{X_{\sim i}}\left(E_{X_i}\left(Y|X_{\sim i}\right)\right)}{V(Y)} = \frac{E_{X_{\sim i}}\left(V_{X_i}\left(Y|X_{\sim i}\right)\right)}{V(Y)} \tag{19}$$

where S_{Ti} denotes the total sensitivity index of ith input parameter.

The S_{Ti} is usually calculated by Monte-Carlo simulation. The process of the calculation is described detailedly in [34]. Saltelli *et al.* assume that there are two independent sampling matrices $\boldsymbol{A}^{m\times n}$ and $\boldsymbol{C}^{m\times n}$, where m is the number of samples

and n is the number of model's input parameters. The new matrix $\boldsymbol{A}_C^{(i)}$ formed by all columns of $\boldsymbol{A}$ except the ith column which is taken from $\boldsymbol{C}$. S_{Ti} can be computed as [34]:

$$S_{Ti} = \frac{\frac{1}{2m}\sum_{j=1}^{m}\left(g(\boldsymbol{A})_j - g\left(\boldsymbol{A}_C^{(i)}\right)_j\right)^2}{V\left(g\left(\boldsymbol{A}\right)\right)} \tag{20}$$

where $(\boldsymbol{A})_j$ and $\left(\boldsymbol{A}_C^{(i)}\right)_j$ denote the j_{th} row of matrix $(\boldsymbol{A})_j$ and $\left(\boldsymbol{A}_C^{(i)}\right)_j$, $V\left(g\left(\boldsymbol{A}\right)\right)$ is the variance of the model output.

In this paper, we use Sobol sequence to generate sample data for sensitivity analysis [34]. The total sensitivity indices of the parameters of cylinder forward model is calculated. We also perform the sensitivity analysis on the principal axes polarizability. Formula (9) and (10) are used as the model function of the principal axes polarizability. The process of sensitivity analysis in this paper is shown in Fig.4 and the results of sensitivity analysis are shown in next section.

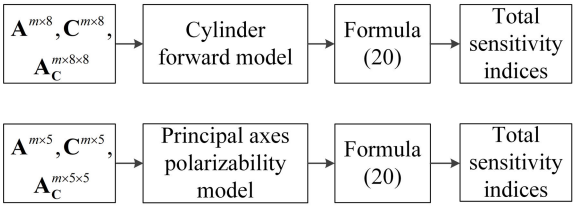

FIGURE 4. Process of sensitivity analysis.

In the Fig. 4, the sampling matrices are generated by Sobol sequence. The cylinder forward model has 8 input parameters and the principal axes polarizability model has 5 input parameters. we use the sampling matrices as the input of these two models. The Formula (20) is used to calculate the total sensitivity indices.

B. INVERSE SENSITIVITY ANALYSIS

Inverse sensitivity analysis determines the probability distribution of model inputs which produces a known distribution of outputs. This method uses probability distributions to describe the uncertainty over inputs and outputs. In [35], Ben Lambert *et al.* describe a computational Monte Carlo method that allows efficient sampling from the input posterior distribution. Consider a model output is $Y = g\left(\boldsymbol{X}\right)$, where $\boldsymbol{X} = (X_1, X_2, \ldots, X_n)$ is input vector. The posterior input distribution is [35]:

$$p\left(\boldsymbol{X}|data\right) \propto \frac{1}{V\left(g\left(\boldsymbol{X}\right)\right)} \cdot p\left(g\left(\boldsymbol{X}\right)|data\right) \tag{21}$$

where *data* denotes a collection of output data points, $v\left(g\left(\boldsymbol{X}\right)\right)$ is the contour volume density at an output value of $g\left(\boldsymbol{X}\right)$. The density distribution of $V\left(g\left(\boldsymbol{X}\right)\right)$ is obtained by kernel density estimation of the model output that produced by independent sampling of the inputs uniformly within their bounds. $p\left(g\left(\boldsymbol{X}\right)|data\right)$ denotes the probability density of $g\left(\boldsymbol{X}\right)$ under the distribution of a given *data*. The Metropolis-Hastings sampling, one of Markov Chain Monte Carlo (MCMC) methods, is used to sample the each input distribution from the posterior input distribution. The pseudocode of inverse sensitivity analysis is described in Alg. 1:

Algorithm 1 Inverse Sensitivity Analysis

Input: A collection of output data points *data*.

Output: Sample values of each input parameter $X^1, X^2, \ldots, X^{N_2}$.

Procedure of contour volume density estimation:

for $i = 1$ to N_1 **do**
  $X^i \sim U(low, high)^n$: sample uniformly within boundaries of input space.
  $Y^i = g\left(X^i\right)$
  $\left(Y^1, Y^2, \ldots, Y^{N_1}\right) \sim V\left(Y\right)$: fit kernel density estimator to output values.
end for

Procedure of Metropolis-Hastings sampling:

Initialize X^0.
for $i = 1$ to N_2 **do**
  $X^{i'} \sim \mathcal{N}\left(X^{i-1}, 0.1\right)$: propose new parameter values for inputs.
  $r = \min\left(\frac{V(g(X^i))p\left(g\left(X^{i'}\right)|data\right)}{V\left(g\left(X^{i'}\right)\right)p(g(X^i)|data)}, 1\right)$: calculate acceptance probability
  $u \sim U\left(0, 1\right)$
  if $r > u$ **then**
    $X^i = X^{i'}$: accept proposal
  else
    $X^i = X^{i-1}$: reject proposal
  end if
end for
return $X^1, X^2, \ldots, X^{N_2}$

C. NUMERICAL OPTIMIZATION ALGORITHMS

After establishing the objective function based on the forward model and observed data, the objective function can be minimized by the numerical optimization algorithms. The numerical optimization algorithms find the optimal solution $\boldsymbol{x}^*$ of the objective function by updating the initial value of the parameter $\boldsymbol{x}_0$ iteratively. The form of iteration is [36]:

$$\boldsymbol{x}_{k+1} = \boldsymbol{x}_k + \alpha_k \boldsymbol{p}_k \tag{22}$$

where the positive scalar α_k is called the step length and the vector $\boldsymbol{p}_k$ is the search direction. The search directions of the gradient descent, steepest descent, Newton's method, BFGS algorithm, conjugate gradient method and LM algorithm are introduced at first, then, the step length selection algorithms are introduced.

1) GRADIENT DESCENT AND STEEPEST DESCENT

The gradient descent and the steepest descent use the negative gradient direction as the search direction [37]:

$$\boldsymbol{p}_k = -\nabla f\left(\boldsymbol{x}_k\right) \tag{23}$$

where ∇ is gradient operator. The difference between these two algorithms is that the steepest descent uses the step length selection algorithm to identify the step length, while the step length of the gradient descent is set to a fixed value. Gradient descent and steepest descent have advantages of low computational cost and short run time of each iteration, but they need a large amount of iterations.

2) NEWTON'S METHOD

Newton's method is based on the Newton direction [36]:

$$\boldsymbol{p}_k = -\boldsymbol{H}_k^{-1} \cdot \nabla f(\boldsymbol{x}_k) \tag{24}$$

where $\boldsymbol{H}_k$ denotes the Hessian matrix of $f(\boldsymbol{x}_k)$, the $\boldsymbol{H}_k^{-1}$ denotes the inverse of the Hessian matrix. Newton's method has faster convergence speed than other numerical optimization algorithms. However, for large scale observed data and parameters, the calculation of the inverse of the Hessian matrix can be prohibitively expensive and the Hessian matrix may not reversible.

3) BFGS ALGORITHM

BFGS algorithm is one of the quasi-Newton methods. The quasi-Newton method is proposed to solve the problem of complex inverse operation of the Hessian matrix. The BFGS algorithm calculates a matrix that approximates the inverse of the Hessian matrix. The search direction of the BFGS algorithm is [38]:

$$\boldsymbol{p}_k = -\boldsymbol{D}_k \cdot \nabla f(\boldsymbol{x}_k) \tag{25}$$

where $\boldsymbol{D}_k \approx \boldsymbol{H}_k^{-1}$. The $\boldsymbol{D}_k$ must satisfy the quasi-Newton condition:

$$(\boldsymbol{x}_{k+1} - \boldsymbol{x}_k) = \boldsymbol{D}_k (\nabla f(\boldsymbol{x}_{k+1}) - \nabla f(\boldsymbol{x}_k)) \tag{26}$$

To simplify the notation, the $\boldsymbol{y}_k$ and $\boldsymbol{s}_k$ are defined as:

$$\begin{aligned} \boldsymbol{y}_k &= \nabla f(\boldsymbol{x}_{k+1}) - \nabla f(\boldsymbol{x}_k) \\ \boldsymbol{s}_k &= \boldsymbol{x}_{k+1} - \boldsymbol{x}_k \end{aligned} \tag{27}$$

The calculation of $\boldsymbol{D}_{k+1}$ is:

$$\boldsymbol{D}_{k+1} = \left(\boldsymbol{I} - \frac{\boldsymbol{s}_k \boldsymbol{y}_k^T}{\boldsymbol{y}_k^T \boldsymbol{s}_k}\right) \boldsymbol{D}_k \left(\boldsymbol{I} - \frac{\boldsymbol{y}_k \boldsymbol{s}_k^T}{\boldsymbol{y}_k^T \boldsymbol{s}_k}\right) + \frac{\boldsymbol{s}_k \boldsymbol{s}_k^T}{\boldsymbol{y}_k^T \boldsymbol{s}_k} \tag{28}$$

where $\boldsymbol{I}$ is the identity matrix and $\boldsymbol{D}_0 = \boldsymbol{I}$. The BFGS algorithm is the most popular quasi-Newton method since it needs little computational cost to approximate the inverse of the Hessian matrix.

4) CONJUGATE GRADIENT METHOD

Conjugate gradient method uses conjugate gradient direction. The new conjugate direction is generated as [39]:

$$\boldsymbol{p}_{k+1} = -\nabla f(\boldsymbol{x}_{k+1}) + \rho_{k+1} \boldsymbol{p}_k \tag{29}$$

where $\boldsymbol{p}_k$ is the last search direction and the initial value $\boldsymbol{p}_0$ takes $-\nabla f(\boldsymbol{x}_0)$, Polak and Ribière defined the ρ_{k+1} as [39]:

$$\rho_{k+1} = \frac{\nabla f(\boldsymbol{x}_{k+1})^T (\nabla f(\boldsymbol{x}_{k+1}) - \nabla f(\boldsymbol{x}_k))}{\nabla f(\boldsymbol{x}_k)^T \nabla f(\boldsymbol{x}_k)} \tag{30}$$

Conjugate gradient method is a classic algorithm in numerical optimization methods and it has less computational cost than the Newton's method.

5) LM ALGORITHM

LM algorithm is specifically applied to least squares problems, and it is a variant of the Newton's method. For the form of formula (15), the LM algorithm uses the Jacobian matrix of residual vector $r(\boldsymbol{x})$ to construct the approximation of the Hessian matrix [36]:

$$\boldsymbol{H}_k \approx J(\boldsymbol{x}_k)^T J(\boldsymbol{x}_k) + \lambda_k \boldsymbol{I} \tag{31}$$

where $J(\boldsymbol{x}_k)$ is the Jacobian matrix of residual vector $r(\boldsymbol{x})$ in k_{th} iteration:

$$J(\boldsymbol{x}_k) = \begin{bmatrix} \nabla r_1(\boldsymbol{x}_k)^T \\ \nabla r_2(\boldsymbol{x}_k)^T \\ \vdots \\ \nabla r_w(\boldsymbol{x}_k)^T \end{bmatrix} \tag{32}$$

The $\boldsymbol{I}$ in Formula (31) is the identity matrix, λ_k is the damping parameter that ensures that the constructed matrix is invertible. The search direction of LM algorithm is:

$$\boldsymbol{p}_k = -\left(J(\boldsymbol{x}_k)^T J(\boldsymbol{x}_k) + \lambda_k \boldsymbol{I}\right)^{-1} \nabla f(\boldsymbol{x}_k) \tag{33}$$

6) STEP LENGTH SELECTION

For the gradient descent, the step length needs to be manually set according to the objective function. For the Newton's method and the LM algorithm, the step length is set to 1 by default. For the other algorithms, researchers need to select an appropriate step length during the iteration process to ensure the algorithm convergent. Suppose that the search direction has been determined in the k_{th} iteration. The objective function becomes a function about α:

$$\phi(\alpha) = f\left(\boldsymbol{x}_k + \alpha \boldsymbol{p}_k\right) \tag{34}$$

The ideal choice of α_k is the global minimum of $\phi(\alpha)$, but searching such an α_k is expensive. More practical strategies perform an inexact step length selection to identify the step length. We use the algorithm mentioned on page 59-61 of 'Numerical Optimization' [36] and routine DCSRCH algorithm from MINPACK-2 [40] to search the step length in our experiments. The process of performing numerical optimization algorithms in this paper is shown in Fig.5.

We use the observed data and the forward model to construct the objective function. The numerical optimization algorithms are used to estimate the parameters of the underground metal target. In the process of the optimization algorithms, the initial guess of the metal target's parameters and the maximum number of iterations are initialized at first. Then, the convergence judgment is performed. If the optimization algorithm does not converge, the search direction and step length are calculated. When the current gradient satisfies the convergence condition, the algorithm output the optimal estimate of the underground metal target's properties.

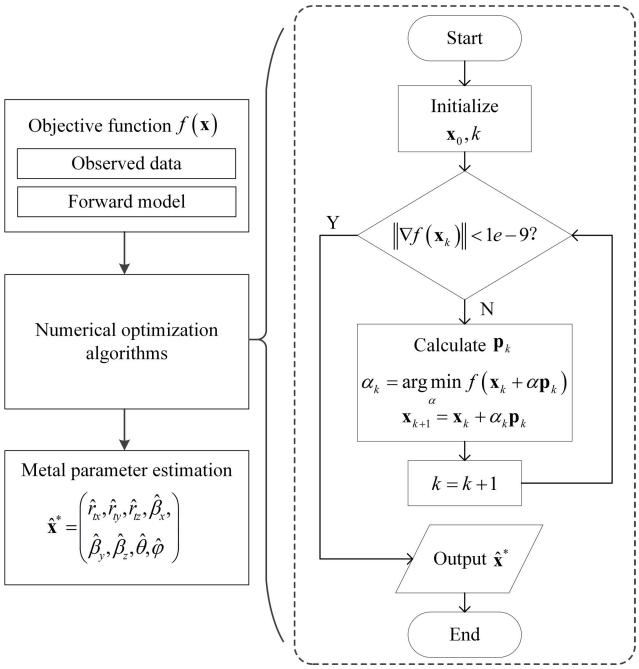

FIGURE 5. Process of performing numerical optimization algorithm.

IV. SIMULATION RESULTS

We built a simulation platform to compare the performances of numerical optimization algorithms. The process of the simulation platform is shown in Fig. 6.

The simulation parameters need to be set first. The simulation parameters include transmitter parameters, metal target parameters and data acquisition parameters. Then, the simulated observed data are obtained by adding noise to the original data generated by the forward model. The metal target parameters are estimated by different numerical optimization algorithms and the absolute errors of the estimation results are calculated. The default simulation parameters are set as shown in Table 1, 2 and 3.

An example of the observed data generated by simulation platform is shown in Fig. 7.

Different colors denote the different secondary field strength. Fig.7(a) shows the detection scenario, Fig.7(b) shows the secondary field strength of z-axis, Fig.7(c) shows the secondary field strength of x-axis and Fig.7(d) shows the secondary field strength of y-axis. It can be seen from the example of the observed data, the strength of the secondary field on the z axis is much greater than the strength of the secondary field on the x and y axes.

TABLE 1. Default values of the transmitter parameters.

Parameter	Description	Default value	Unit
a_d	Radius of transmit coil	0.4	m
I_0	Amplitude of current	20	A
f	Frequency of current	1000	Hz

TABLE 2. Default values of the metal target parameters.

Parameter	Description	Default value	Unit
$\boldsymbol{r}_d$	Position vector of metal target	$[0, 0, -4]$	m
a	Radius of metal target	0.1	m
L	Length of metal target	0.8	m
σ	Conductivity of metal target	5.71×10^7	S/m
μ	Permeability of metal target	$4\pi \times 10^{-7}$ H/m	
θ	Pitch angle of metal target	90	$Degree$
φ	Roll angle of metal target	0	$Degree$

TABLE 3. Default values of the data acquisition parameters.

Parameter	Description	Default value	Unit
l	Spacing of data acquisition	0.5	m
SNR	Signal to noise ratio	20	dB

A. SENSITIVITY ANALYSIS FOR CYLINDER FORWARD MODEL

We calculated total sensitivity indices of the parameters in the z axis of the cylinder forward model. The position of the detector is fixed at the $[0, 0, 0]^T$ so that the secondary field is only related to the metal target's properties. The range of values of each parameter are shown in Table 4.

TABLE 4. Parameter range of the forward model.

Parameter	Description	Range	Unit
r_{tx}	x coordinate of metal target	$[-2, 2]$	m
r_{ty}	y coordinate of metal target	$[-2, 2]$	m
r_{tz}	z coordinate of metal target	$[-5, -1]$	m
β_x	x-axis polarizability of metal target	$[0.01, 0.05]$	/
β_y	y-axis polarizability of metal target	$[0.01, 0.05]$	/
β_z	z-axis polarizability of metal target	$[0.04, 0.14]$	/
θ	Pitch angle of metal target	$[-180, 180]$	$degree$
φ	Roll angle of metal target	$[-180, 180]$	$degree$

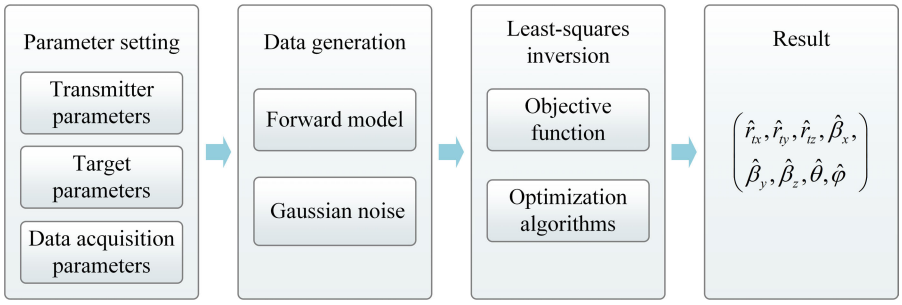

FIGURE 6. Process of the simulation platform.

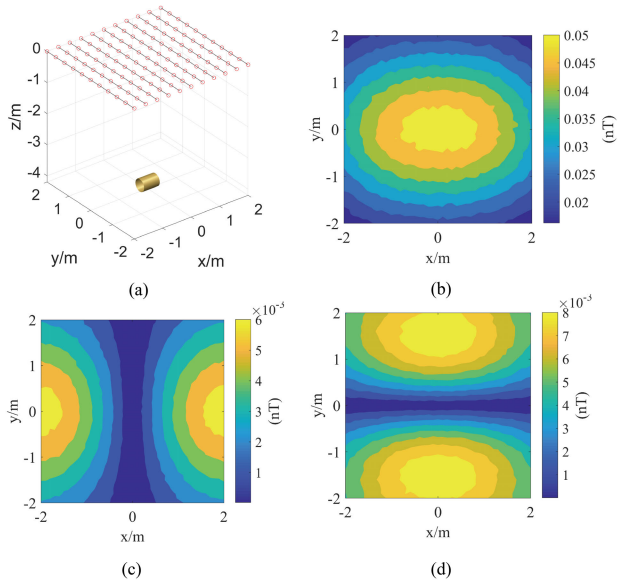

FIGURE 7. A set of triaxial observed data generated by simulation platform. (a) The detection scenario; (b) The secondary field strength of z-axis; (c) The secondary field strength of x-axis; (d) The secondary field strength of y-axis.

50000 samples are generated by Sobol sequence and the Formula (20) is used to calculate the total sensitivity indices of each parameter. The results are shown in Fig. 8.

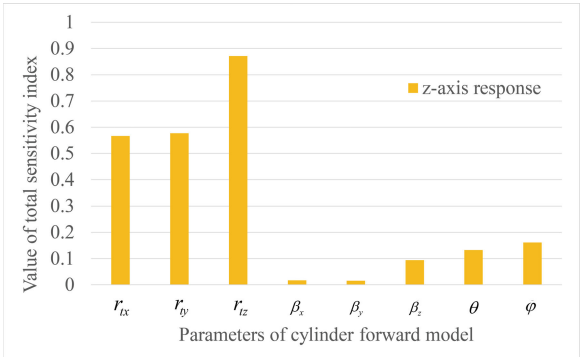

FIGURE 8. Sensitivity results of the cylinder forward model.

The larger the total sensitivity index, the greater the influence of parameters on the model output. Fig.8 shows that the total sensitivity indices of the positions are much greater than that of other parameters and the total sensitivity indices of orientation are greater than that of principal axes polarizability. The result indicates that the distance between the metal target and the detector has a great influence on the secondary field and the depth of the metal target most affects secondary field response.

B. INVERSE SENSITIVITY ANALYSIS FOR CYLINDER FORWARD MODEL

In the inverse sensitivity analysis, the position of the detector is also fixed at the $[0, 0, 0]^T$. We set the metal target parameters as shown in Table 5 and get the secondary field values of z axis $B_{sz} = 0.0198$. The distribution of the z axis output is set to $\mathcal{N}(0.0198, 0.005)$. $N1$ is set to 10000 and $N2$ is set to 50000. The results of inverse sensitivity analysis are shown in Fig. 9.

TABLE 5. Metal target parameters of inverse sensitivity analysis.

Parameter	Description	Range	Unit
r_{tx}	x coordinate of metal target	0	m
r_{ty}	y coordinate of metal target	0	m
r_{tz}	z coordinate of metal target	-3	m
β_x	x-axis polarizability of metal target	0.0128	/
β_y	y-axis polarizability of metal target	0.0128	/
β_z	z-axis polarizability of metal target	0.045	/
θ	Pitch angle of metal target	0	$degree$
φ	Roll angle of metal target	0	$degree$

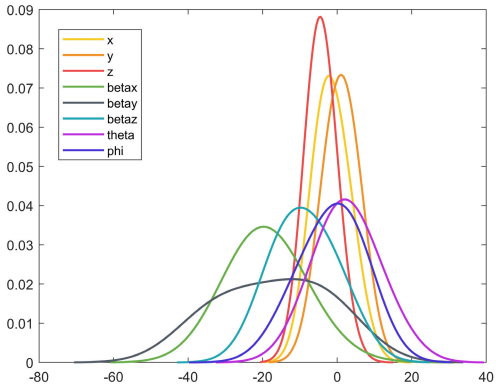

FIGURE 9. Inverse sensitivity analysis result of the cylinder forward model.

It can be seen from Fig.9, the distributions of input parameters of forward model are sampled by inverse sensitivity analysis. The variance of the distribution of target's position is less than the variance of the distribution of the other properties. From the result of the inverse sensitivity analysis, we can learn that the uncertainty of the position parameter is the smallest among the all parameters in the forward model, and accuracy of the target's position estimated by optimization algorithms will also be highest. The estimation accuracy comparison of different target's parameters is performed in IV-C3.

C. COMPARISON OF THE NUMERICAL OPTIMIZATION ALGORITHMS

The performances of numerical optimization algorithms under different SNRs and different amounts of observed data are compared, respectively. The performance of the algorithms is discussed from five aspects: estimation error of the position, estimation error of the principal axes polarizability, estimation error of the orientation, number of iterations and run time. The estimation error of the position is defined as the average of estimation errors of the x, y and z coordinates. The estimation error of the magnet polarizability is defined as the average of estimation errors of three principal axes polarizabilities. The estimation error of orientation is defined

as the average of estimation errors of the pitch angle and the roll angle. We set up five detection scenarios and the average estimation error of each optimization algorithm in the five scenarios is compared. The parameters of metal targets in the five scenarios are shown in Table 6.

TABLE 6. Metal target parameters of five detection scenarios.

Detection scenario	Position	Pitch angle	Roll angle
1	$[0, 0, -3]$	0	0
2	$[0, 1, -3]$	10	50
3	$[0, -1, -3]$	10	50
4	$[-1, 1, -3]$	70	40
5	$[-1, -1, -3]$	70	40

The simulation platform is implemented in MATLAB and run on a PC featuring Intel Core i5-3470 CPU (3.2 GHz) and 12 GB of RAM.

1) PERFORMANCE COMPARISON UNDER DIFFERENT SNRs

In this experiment, the data acquisition spacing is set to 0.5m as default. The performances of four numerical optimization algorithms under different SNR are shown as follows. The algorithms do not include the gradient descent and Newton's method. Although each iteration of gradient descent is fast, it takes hundreds of thousands of iterations to converge. And it is time-consuming to identify a step length manually. In the Newton's method, the Hessian matrix will be singular in iteration process, which causes the algorithm to fail to converge. Therefore, the gradient descent and the Newton's method are not suitable for underground metal detection.

Fig. 10, Fig. 11 and Fig. 12 show that the accuracy of these algorithms increases with the increase of SNR. When the SNR is greater than or equal to 20*dB*, the estimation error of the position is less than 2 *cm*, the estimation error of the principal axes polarizability is less than 0.001, the estimation error of the orientation is less than 2 *degree*. The estimation errors of different algorithms are extremely similar because the algorithms stop iterating when the gradient of the objective function satisfies the same terminal condition. The differences between these algorithms are the number of iterations and the run time. As shown in Fig. 13 and Fig. 14,

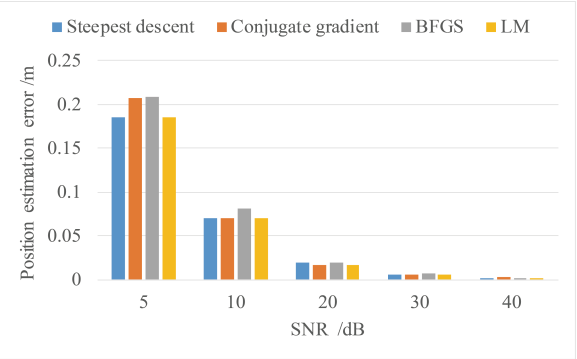

FIGURE 10. Comparison of position estimation error under different SNR.

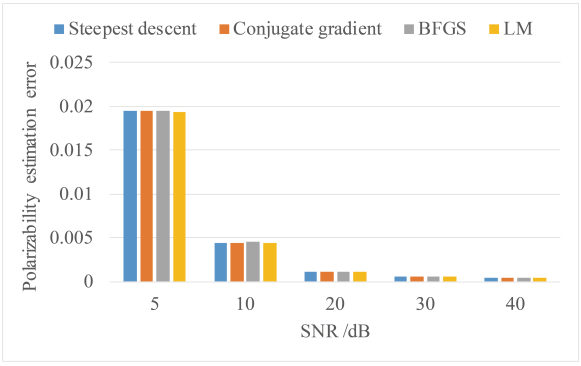

FIGURE 11. Comparison of polarizability estimation error under different SNR.

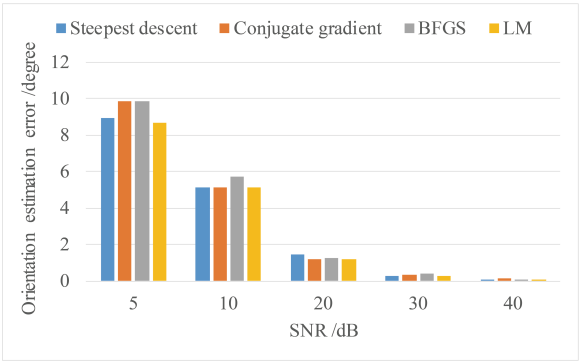

FIGURE 12. Comparison of orientation estimation error under different SNR.

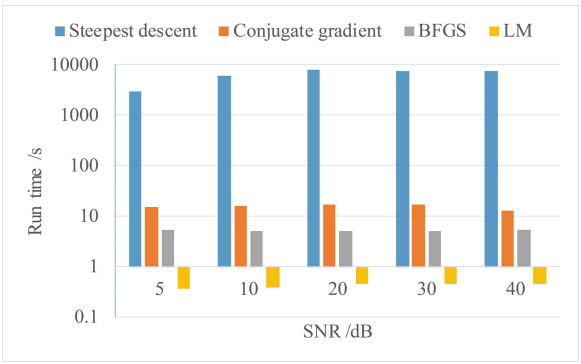

FIGURE 13. Comparison of run time of numerical optimization algorithms under different SNR.

The steepest descent algorithm takes the longest run time and maximum number of iterations. The run time and number of iterations of the steepest descent are around 2 hours and 200000 iterations. The run time and number of iterations of the conjugate gradient algorithm are less than 17 seconds and 428 iterations. The run time and number of iterations of the BFGS algorithm are less than 5.4 seconds and 150 iterations. The LM algorithm has the best performance, and it only takes 0.5 seconds and around 38 iterations to get the result.

The results of the performance comparison under different SNRs indicate that the accuracy of the numerical optimization

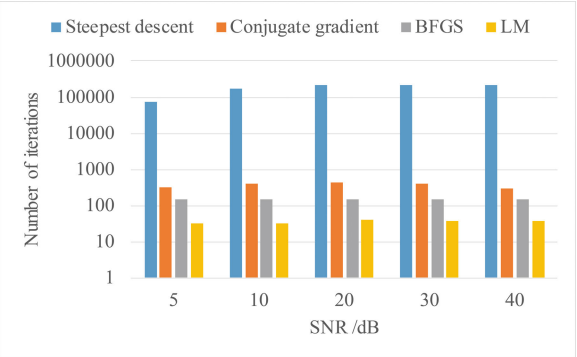

FIGURE 14. Comparison of iterations of numerical optimization algorithms under different SNR.

algorithms is sensitive to the noise. With the increase of SNR, the accuracy of the optimization algorithms increase rapidly. The steepest descent takes a large amounts time to converge, which is not suitable for underground metal target detection. The LM algorithm has the shortest run time under all SNR conditions.

2) PERFORMANCE COMPARISON UNDER DIFFERENT DATA ACQUISITION SPACINGS

In this experiment the SNR is set to $20dB$ as default. The detection area is $4m * 4m$ as shown in Fig. 1. Five data acquisition spacings are set in the experiment. The data acquisition spacings are $0.9m$, $0.7m$, $0.5m$, $0.3m$, and $0.1m$. The amount of training data corresponding to these acquisition spacings is 75, 108, 243, 588, 5043 sets of data, respectively. The performances of four numerical optimization algorithms are shown in Fig. 15-19.

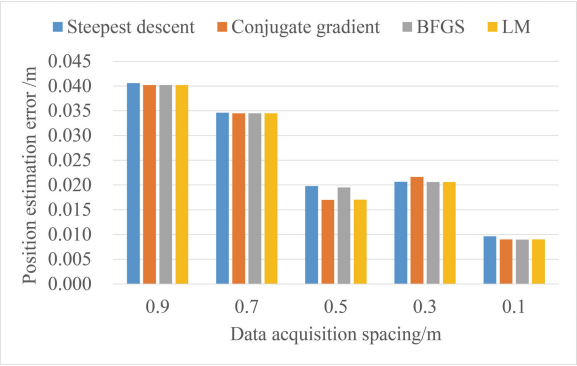

FIGURE 15. Comparison of position estimation error under different acquisition spacings.

In Fig. 15, Fig. 16 and Fig. 17, the accuracy of these algorithms shows an upward trend with the decrease of the data acquisition spacing. When the spacing is $0.1m$, the position estimation error is less than $0.9cm$, the principal axes polarizability estimation error is less than 0.0006, the orientation estimation error is less than 0.6 *degree*. These results indicate that the smaller acquisition spacings can increase the detection accuracy. However, the run time of the algorithm also increases exponentially as the spacing decreases. As shown

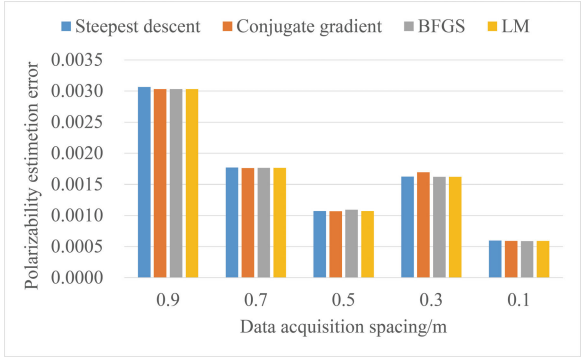

FIGURE 16. Comparison of polarizability estimation error under different acquisition spacings.

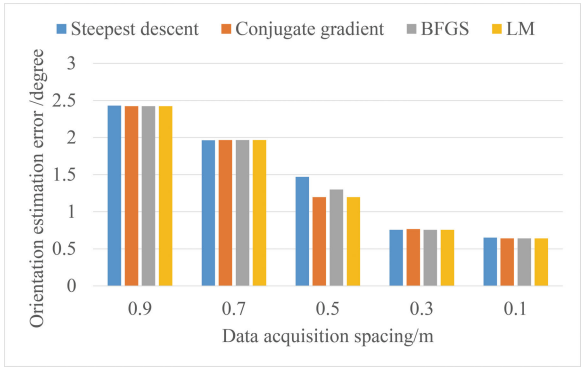

FIGURE 17. Comparison of orientation estimation error under different acquisition spacings.

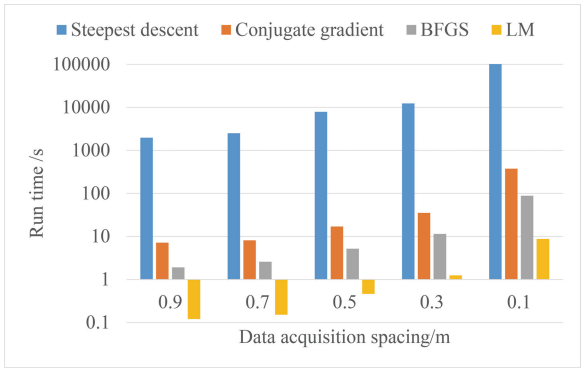

FIGURE 18. Comparison of run time of numerical optimization algorithms under different acquisition spacings.

in Fig. 18, the run time of the steepest descent algorithm reached 38 hours when the spacing is $0.1m$. The run time of the conjugate gradient algorithm reached 376 seconds. The run time of the BFGS algorithm reached 88 seconds. The run time of the LM algorithm is from 0.12 seconds to 8.7 seconds.

3) ESTIMATION ACCURACY COMPARISON OF DIFFERENT TARGET PARAMETERS

To verify the results of the inverse sensitivity analysis, we compare the estimation accuracy of different target's parameters. We use the same target's parameters as the inverse sensitivity analysis and repeatedly run the

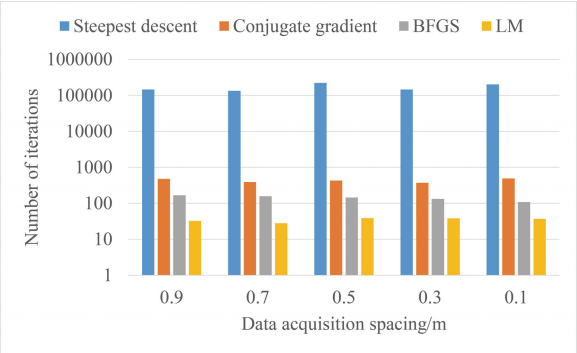

FIGURE 19. Comparison of iterations of numerical optimization algorithms under different acquisition spacings.

LM algorithm 1000 times. The obtained result are the distribution of estimate values of each parameter. We use Formula (35) to normalize the estimate values:

$$x_{new} = \frac{x - x_{min}}{x_{max} - x_{min}} \tag{35}$$

where x_{new} is the normalized value, x_{min} and x_{max} are the minimum and maximum values of the value range of z, and the value range corresponds to Table 4. The normalized distribution is shown in Fig. 9.

It can be seen from Fig.20 that the variance of the estimation of the z-axis position is the smallest. The estimated value distributions of x-axis and y-axis are similar and their variance is greater than the variance of z-axis estimated value distribution. The variance of the estimated values of other parameters is relatively large. The larger the variance, the higher the uncertainty of the parameter. This result indicates that the accuracy of position estimation is higher than that of orientation and principal axis polarizability and this result is consistent with the result of inverse sensitivity analysis.

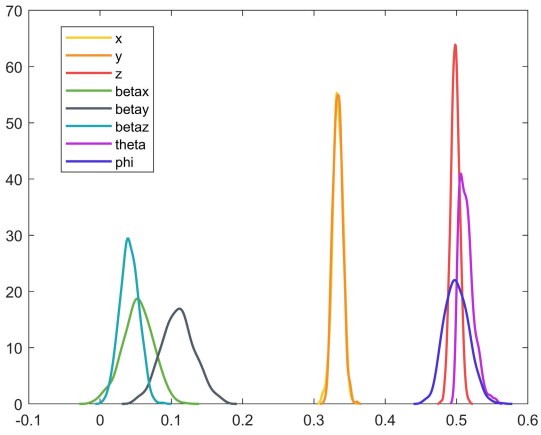

FIGURE 20. Normalized distribution of different parameters estimation.

4) DETAILED TIME CONSUMPTION OF THE OPTIMIZATION ALGORITHMS

According to experiments and results, the LM algorithm has the best performance and the performance of the steepest descent is the worst. We further analyzed the detailed time consumption of these algorithms. We take the second set of detection scenarios as an example and the SNR and data acquisition spacing are set to $20dB$ and $0.5m$, respectively. The results are shown in Table 7.

TABLE 7. Detailed time consumption of numerical optimization algorithms.

Algorithms	Run time of each iteration	Number of iterations
Steepest descent	$0.035s$	122703
Conjugate gradient	$0.039s$	408
BFGS	$0.036s$	128
LM	$0.027s$	25

The run time of steepest descent, conjugate descent method and BFGS algorithm is similar and the computational cost mainly spent in three parts: search direction calculation, step length selection and convergence judgment. The convergence judgment refers to using the gradient of the objective function to judge whether the algorithm converges. The run time of the three parts in steepest descent is $0.01s$, $0.012s$ and $0.009s$, respectively. The run time of the three parts in conjugate gradient method is $0.012s$, $0.013s$ and $0.009s$, respectively. The run time of the three parts in BFGS algorithm is $0.012s$, 0.012s and 0.009s, respectively. We found that the most time-consuming operation in the three parts is the calculation of gradient. For the LM algorithm, it does not require the step length selection. The run time of the search direction calculation and convergence judgment of LM algorithm is $0.015s$ and $0.009s$, respectively. These results indicate that the most significant difference between these algorithms is the search direction. The search direction of LM algorithm has the fastest convergence speed. In addition, the gradient calculation and step length selection greatly affect the efficiency of the algorithms.

V. CONCLUSION

Overall, we gave the results of the variance-based sensitivity analysis and the inverse sensitivity analysis of the cylinder forward model and the results of the performance comparison of six numerical optimization algorithms in underground metal detection. The results of sensitivity analysis indicate that the influence of the position of the metal target on the secondary field is much greater than the influence of the principal axes polarizability and orientation of the metal target on the secondary field, and the depth of the metal target has the great influence on the secondary field. The inverse sensitivity analysis results indicate that the position of the target estimated by the optimization algorithms is more accurate than that of the principal axes polarizability and orientation. The results of optimization algorithms comparison show that the gradient descent, steepest descent and the Newton's method are not suitable for underground metal detection. The BFGS algorithm, conjugate gradient method and LM algorithm can efficiently estimate the properties of underground metals. The LM algorithm has a shorter run time

and a less number of iterations than the other numerical optimization algorithms in underground metal target detection. We compared the performance of the optimization algorithms under different SNRs. The results show that the accuracy of the optimization algorithms is greatly affected by noise. With the increase of SNR, the accuracy of the optimization algorithms increase rapidly. We also compared the performance of the optimization algorithms under different amounts of observed data. The results show that more observed data can improve the accuracy of inversion, but the efficiency of inversion also decreases greatly. Our experimental data also gives researchers a reference to do a trade-off between the inversion accuracy and inversion efficiency. Finally, We further analyze the detailed time consumption of each algorithm. The gradient calculation and step length selection greatly affect the efficiency of the algorithms. In the future work, we will concentrate on improving the efficiency of the step length selection algorithm and the parallel computing of the gradient calculation.

REFERENCES

[1] S. Chen, S. Zhang, J. Zhu, and X. Luan, "Accurate measurement of characteristic response for unexploded ordnance with transient electromagnetic system," *IEEE Trans. Instrum. Meas.*, vol. 69, no. 4, pp. 1728–1736, Apr. 2019.

[2] T. N. I. Alrumaih, "The construction of a robotic vehicle metal detector as a tool for searching archaeology sites," in *Proc. 1st Int. Conf. Comput. Appl. Inf. Secur. (ICCAIS)*, Apr. 2018, pp. 1–6.

[3] P. Mlambo, H. Dera, E. Chiweshe, and E. Jonathan, "Inductive metal detectors and the design of prospecting robots: A possibility," in *Proc. EAI Int. Conf. Res., Innov. Develop. Afr.* Ghent, Belgium: European Alliance for Innovation, 2018, p. 10.

[4] S. Duan, Y. Li, P. Wang, Y. Wan, L. Xu, and T. Li, "The influence of target orientation on the underground targets classification," in *Proc. IEEE 19th Int. Conf. Commun. Technol. (ICCT)*, Oct. 2019, pp. 487–494.

[5] H. Song, H. Dong, Z. Yuan, J. Zhu, H. Zhang, and Y. Huang, "An EEMD-based electromagnetic induction method for nondestructive testing of buried metal conductors," *IEEE Access*, vol. 7, pp. 142261–142271, 2019.

[6] F. Shubitidze, B. E. Barrowes, and I. Shamatava, "Detection and identification of buried explosive hazards using high frequency EMI sensing," in *Proc. IEEE Int. Geosci. Remote Sens. Symp. (IGARSS)*, Jul. 2018, pp. 6769–6772.

[7] D. Ambrus, D. Vasic, and V. Bilas, "Robust estimation of metal target shape using time-domain electromagnetic induction data," *IEEE Trans. Instrum. Meas.*, vol. 65, no. 4, pp. 795–807, Apr. 2016.

[8] Y. Wan, Z. Wang, P. Wang, Z. Liu, N. Li, and C. Zhang, "An initial value estimation method for the Kalman and extended Kalman filters in underground metal detection," *Appl. Sci.*, vol. 9, no. 19, p. 4113, Oct. 2019.

[9] D. Ambrus, D. Vasic, and V. Bilas, "Comparative study of planar coil EMI sensors for inversion-based detection of buried objects," *IEEE Sensors J.*, vol. 20, no. 2, pp. 968–979, Jan. 2020.

[10] J. Thiesson, A. Tabbagh, F.-X. Simon, and M. Dabas, "3D linear inversion of magnetic susceptibility data acquired by frequency domain EMI," *J. Appl. Geophys.*, vol. 136, pp. 165–177, Jan. 2017.

[11] G. P. Deidda, P. D. de Alba, G. Rodriguez, and G. Vignoli, "Inversion of multiconfiguration complex EMI data with minimum gradient support regularization: A case study," *Math. Geosci.*, pp. 1–26, Feb. 2020.

[12] A. Mester, J. van der Kruk, E. Zimmermann, and H. Vereecken, "Quantitative two-layer conductivity inversion of multi-configuration electromagnetic induction measurements," *Vadose Zone J.*, vol. 10, no. 4, pp. 1319–1330, Nov. 2011.

[13] F. Shubitidze, B. E. Barrowes, J. B. Sigman, K. O'Neill, and I. Shamatava, "UXO classification procedures applied to advanced EMI sensors and models," in *Proc. 21st Int. Seminar/Workshop Direct Inverse Problems Electromagn. Acoustic Wave Theory (DIPED)*, Sep. 2016, pp. 173–177.

[14] M. D. Wigh, T. M. Hansen, and A. Døssing, "Inference of unexploded ordnance (UXO) by probabilistic inversion of magnetic data," *Geophys. J. Int.*, vol. 220, no. 1, pp. 37–58, Jan. 2020.

[15] F. Shubitidze, B. Barrowes, Y. Wang, I. Shamatava, J. Sigman, and K. O'Neill, "Advanced EMI models for survey data processing: Targets detection and classification," *Proc. SPIE*, vol. 9823, Jun. 2016, Art. no. 98230O.

[16] J. P. Fernández, B. E. Barrowes, T. M. Grzegorczyk, N. Lhomme, K. O'Neill, and F. Shubitidze, "A man-portable vector sensor for identification of unexploded ordnance," *IEEE Sensors J.*, vol. 11, no. 10, pp. 2542–2555, Oct. 2011.

[17] T. M. Grzegorczyk, B. E. Barrowes, F. Shubitidze, J. P. Fernandez, and K. O'Neill, "Simultaneous identification of multiple unexploded ordnance using electromagnetic induction sensors," *IEEE Trans. Geosci. Remote Sens.*, vol. 49, no. 7, pp. 2507–2517, Jul. 2011.

[18] W. Rodi and R. L. Mackie, "Nonlinear conjugate gradients algorithm for 2-D magnetotelluric inversion," *Geophysics*, vol. 66, no. 1, pp. 174–187, Jan. 2001.

[19] L. A. Marsh, C. Ktistis, A. Järvi, D. W. Armitage, and A. J. Peyton, "Three-dimensional object location and inversion of the magnetic polarizability tensor at a single frequency using a walk-through metal detector," *Meas. Sci. Technol.*, vol. 24, no. 4, Apr. 2013, Art. no. 045102.

[20] Y. Tao, W. Yin, W. Zhang, Y. Zhao, C. Ktistis, and A. J. Peyton, "A very-low-frequency electromagnetic inductive sensor system for workpiece recognition using the magnetic polarizability tensor," *IEEE Sensors J.*, vol. 17, no. 9, pp. 2703–2712, May 2017.

[21] C. A. Balanis, *Antenna Theory: Analysis and Design*. Hoboken, NJ, USA: Wiley, 2016.

[22] O. A. Abdel-Rehim, J. L. Davidson, L. A. Marsh, M. D. O'Toole, and A. J. Peyton, "Magnetic polarizability tensor spectroscopy for low metal anti-personnel mine surrogates," *IEEE Sensors J.*, vol. 16, no. 10, pp. 3775–3783, May 2016.

[23] T. M. Grzegorczyk and B. E. Barrowes, "Real-time processing of electromagnetic induction dynamic data using Kalman filters for unexploded ordnance detection," *IEEE Trans. Geosci. Remote Sens.*, vol. 51, no. 6, pp. 3439–3451, Jun. 2013.

[24] T. Bell, B. Barrow, J. Miller, and D. Keiswetter, "Time and frequency domain electromagnetic induction signatures of unexploded ordnance," *Subsurf. Sens. Technol. Appl.*, vol. 2, no. 3, pp. 153–175, 2001.

[25] F. Shubitidze, "A complex approach to UXO discrimination: Combining advanced EMI forward models and statistical signal processing," Sky Res., Ashland, OR, USA, Tech. Rep., 2012.

[26] K. Zhang, Z. Lu, D. Wu, and Y. Zhang, "Analytical variance based global sensitivity analysis for models with correlated variables," *Appl. Math. Model.*, vol. 45, pp. 748–767, May 2017.

[27] I. M. Sobol, "Sensitivity estimates for nonlinear mathematical models," *Math. Model. Comput. Exp.*, vol. 1, no. 4, pp. 407–414, 1993.

[28] A. Saltelli, M. Ratto, T. Andres, F. Campolongo, J. Cariboni, D. Gatelli, M. Saisana, and S. Tarantola, *Global Sensitivity Analysis: The Primer*. Hoboken, NJ, USA: Wiley, 2008.

[29] X. Sun, S. Roberts, B. Croke, and A. Jakeman, "A comparison of global sensitivity techniques and sampling method," in *Proc. 22nd Int. Congr. Modelling Simulation*, Hobart, TAS, Australia, 2017, pp. 57–63.

[30] W. Yun, Z. Lu, K. Zhang, and X. Jiang, "An efficient sampling method for variance-based sensitivity analysis," *Structural Saf.*, vol. 65, pp. 74–83, Mar. 2017.

[31] T. Locatelli, S. Tarantola, B. Gardiner, and G. Patenaude, "Variance-based sensitivity analysis of a wind risk model–model behaviour and lessons for forest modelling," *Environ. Model. Softw.*, vol. 87, pp. 84–109, Jan. 2017.

[32] T. Homma and A. Saltelli, "Importance measures in global sensitivity analysis of nonlinear models," *Rel. Eng. Syst. Saf.*, vol. 52, no. 1, pp. 1–17, 1996.

[33] N. A. Weiss, *A Course in Probability*. Reading, MA, USA: Addison-Wesley, 2006.

[34] A. Saltelli, P. Annoni, I. Azzini, F. Campolongo, M. Ratto, and S. Tarantola, "Variance based sensitivity analysis of model output. Design and estimator for the total sensitivity index," *Comput. Phys. Commun.*, vol. 181, no. 2, pp. 259–270, Feb. 2010.

[35] B. Lambert, D. Gavaghan, and S. Tavener, "Inverse sensitivity analysis of mathematical models avoiding the curse of dimensionality," *BioRxiv*, 2018, Art. no. 432393.

[36] J. Nocedal and S. Wright, *Numerical Optimization*. Springer, 2006.

[37] S. Ruder, "An overview of gradient descent optimization algorithms," 2016, *arXiv:1609.04747*. [Online]. Available: http://arxiv.org/abs/1609.04747
[38] Y. Rao and Y. Wang, "Seismic waveform tomography with shot-encoding using a restarted L-BFGS algorithm," *Sci. Rep.*, vol. 7, no. 1, pp. 1–9, Dec. 2017.
[39] B. Keshtegar, "Limited conjugate gradient method for structural reliability analysis," *Eng. Comput.*, vol. 33, no. 3, pp. 621–629, Jul. 2017.
[40] B. Averick, G. Richard, and J. Moré, "Minpack-2 project," Argonne Nat. Lab., Lemont, IL, USA, Tech. Rep., 1993.

YADONG WAN received the B.E. and Ph.D. degrees from the University of Science and Technology Beijing, in 2003 and 2010, respectively. He was a Visiting Scholar with the Worcester Polytechnic Institute in area of wireless location, from August 2012 to February 2013. His current research interests include underground target detection, industrial wireless sensor networks, signal processing, and data science of materials genome initiative.

ZHEN WANG received the B.E. degree from the North China Institute of Aerospace Engineering, in 2018. He is currently pursuing the master's degree with the School of Computer and Communication Engineering, University of Science and Technology Beijing, China. His current research interests include underground target detection and optimization algorithm.

PENG WANG received the B.E. and Ph.D. degrees from the University of Science and Technology Beijing, in 2012 and 2018, respectively. His current research interests include underground target detection, low frequency wireless communication, wireless sensor networks, adaptive signal processing, and near field electromagnetic localization.

CHAO ZHANG received the master's degree in physics and the Ph.D. degree in material science and engineering from the University of Science and Technology Beijing, in 2003 and 2018, respectively. He has been began the study of magnetic sensor, since 2006. His current research interest includes weak magnetic field detection systems.

SHIHONG DUAN received the B.E. and Ph.D. degrees in pattern recognition and computer science from the University of Science and Technology Beijing (USTB), China, in 1998 and 2012, respectively. She was an Assistant Professor with the School of Computer and Communication Engineering, USTB, from January 1998 to June 2013, where she has been an Associate Professor, since July 2013. From August 2014 to August 2015, she was a Visiting Scholar with the Center for Wireless Information Network Studies, Department of Electrical and Computer Engineering, Worcester Polytechnic Institute. Her research interests include wireless channel study, human activity recognition, mobile robotics, and underground target detection.

NA LI received the B.E. and Master of Science degrees from the University of Science and Technology Beijing, China, in 2001 and 2006, respectively. She began to work at the University of Science and Technology Beijing, in 2006. Her current research interests include multivariate statistical analysis, statistical learning theory, and machine learning.